The design of a compliant shape-preserving ring

Schreurs, K. W.A.; Radaelli, G.; Alijani, F.

DOI
10.1016/j.mechmachtheory.2020.103918

Publication date
2020

Document Version
Final published version

Published in
Mechanism and Machine Theory

Mechanism and Machine Theory 151 (2020) 103918

Contents lists available at ScienceDirect

Mechanism and Machine Theory

journal homepage: www.elsevier.com/locate/mechmachtheory

Research paper

The design of a compliant shape-preserving ring

K.W.A. Schreurs, G. Radaelli*, F. Alijani

Dept. of Precision and Microsystems Engineering Delft University of Technology, Mekelweg 2, CD 2628 Delft, the Netherlands

ARTICLE INFO

Article history:
Received 13 December 2019
Revised 28 February 2020
Accepted 12 April 2020

Keywords:
Compliant mechanisms
Shape-preservation
Flexures
Shape optimization
Dilational mechanisms

ABSTRACT

Compliant shape-preserving mechanisms fill a small niche within the established research field of compliant mechanisms. To date no report exists on a compliant shape-preserving ring, even though these mechanisms can give rise to a multitude of practical applications. They can essentially act as novel sealing mechanisms, compliant grippers or find use in medical applications. This paper presents three compliant shape-preserving rings that maintain their circular shape up to 99% for their full range-of-motion. The best design can expand in diameter by $\approx 45\%$. A prototype of a compliant shape-preserving ring was constructed from PETG (Polyethylene Terephtalate Glycol-modified) using fused-filament-fabrication. The experimental evaluation of this prototype showed a good agreement with the numerical model describing the design. A novel compliant scissor mechanism was obtained in the design process and this mechanism can prove useful in the design of other compliant shape-preserving mechanisms.

1. Introduction

Shape-preserving mechanisms, also known as dilational mechanisms [1], are expanding mechanisms that preserve their shape upon expansion. There has been an interest in these types of mechanisms for a long time and in particular shape-preserving mechanisms based on linkages have been studied many times within the field of deployable structures [2,3].

The first well known shape-preserving mechanism was designed by Hoberman [4], see Fig. 1. He invented a radially foldable linkage based on scissor mechanisms with angled links. This concept was later extended by You and Pellegrino [5] with the notion of the 'generalized angulated element'. Symmetric examples of these elements can be used to construct closed loop foldable linkages with shape-preserving properties that can move through a large range-of-motion. A different class of shape-preserving mechanisms was developed by Wohlhart [6,7], who formed expanding polyhedra by combining multiple planar mechanisms, and Wei et al. [8] who worked on polyhedral mechanism formed by spatial links. Other approaches are based on scalable polygonal units, such as the work of Kiper et al. [9,10] or more recently Broeren et. al[1].

Compliant mechanisms have particular advantages that could open new windows in the design of shape-preserving structures, namely reduced wear due to the absence of frictional elements and increased potential for miniaturization [11]. Even though many conventional shape-preserving mechanisms have been proposed and a few compliant examples exist [12–15] there has to date not been any reports on the design of an annular compliant shape-preserving mechanism. That

* Corresponding author.
E-mail addresses: G.Radaelli@tudelft.nl (G. Radaelli), F.Alijani@tudelft.nl (F. Alijani).

https://doi.org/10.1016/j.mechmachtheory.2020.103918

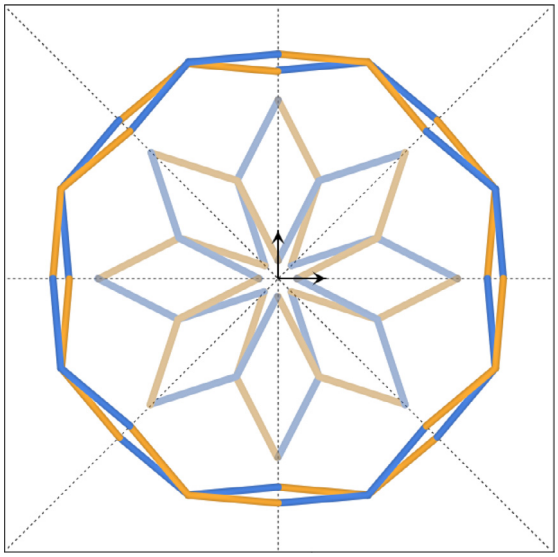

Fig. 1. An example of a linkage designed by Hoberman. The linkage is shown in a folded and expanded configuration.

is while these types of mechanisms can essentially act as novel sealing mechanisms, compliant grippers, or stent-grafts for the medical industry.

To realize such applications, a large range of motion of these shape-preserving mechanisms is required and hence the aim of this work is to design a compliant shape-preserving ring that has a range of motion similar to the radially foldable linkages described above. To this end, a new compliant scissor mechanism is designed, which is then used as a building block for a shape-preserving compliant ring. The ring is completed by attaching the scissors in a periodic fashion which results in a compliant mechanism with a behaviour similar to the linkage designed by Hoberman.

The scissor mechanism comprises a set of curved flexures with a constant rectangular cross section. A shape optimization procedure is then used to form these flexures in such a way that the compliant ring has a shape-preserving behaviour. A prototype of this ring was designed and fabricated from PETG filament using a fused-filament-fabrication (FFF) 3D-printer and its performance was evaluated experimentally.

The structure of the paper reads as follows. Section 2 presents the design goals, shows an analysis of the kinematics of a radially foldable linkage and explains the methods used in the design process. Section 3 presents the obtained designs, evaluates their performance and discusses the results, while Section 4 concludes the paper.

2. Methods

This section describes the methods that were used in the design process. First the desired design features are explained and the kinematics of a radially foldable linkage are analysed. Next, details are provided on the compliant design, the optimization procedure, fabrication and testing.

2.1. Design features

The key feature of the design is its shape-preserving behaviour. Hence, the aim is to design a mechanism for which the shape of the circumscribed circle through the mechanism endpoints is preserved upon a uni-axial straining of the mechanism. In order to evaluate the circularity of the shape a metric called the 'aspect ratio' was defined. This aspect ratio ξ is defined as the ratio between the radius of the mechanism measured along the x-axis r_x and the radius of the mechanism measured along the y-axis r_y, as illustrated in Fig. 2 (a).

$$\xi = \frac{r_x}{r_y}. \tag{1}$$

Ideally the aspect ratio should remain equal to unity upon expansion of the mechanism, as this ensures that the mechanism expands at equal rates along both the x and y axes which allows it to maintain a circular shape.

Since the mechanism should be compliant, no sliding contacts, no conventional bearings and no rolling contacts can be used in the design. All movements should be allowed for by elastic deformation of the mechanism.

The third important feature regarding the design is the range-of-motion (*ROM*) of the mechanism. The *ROM* is comprised of the ratio between the radius of the mechanism in its expanded state versus the radius in its initial state. This radius is

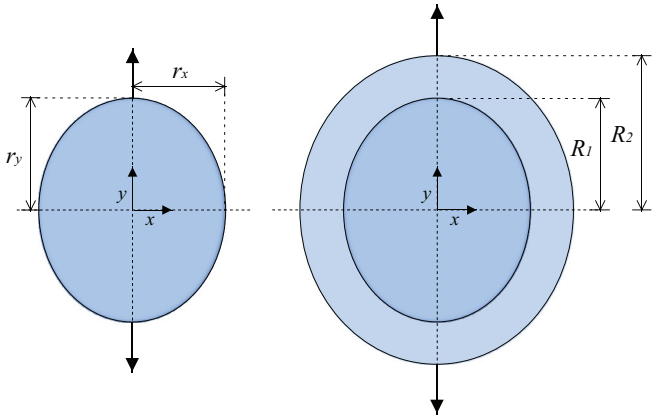

Fig. 2. (a) aspect ratio defined as r_x/r_y. (b) Range of motion defined as R_2/R_1.

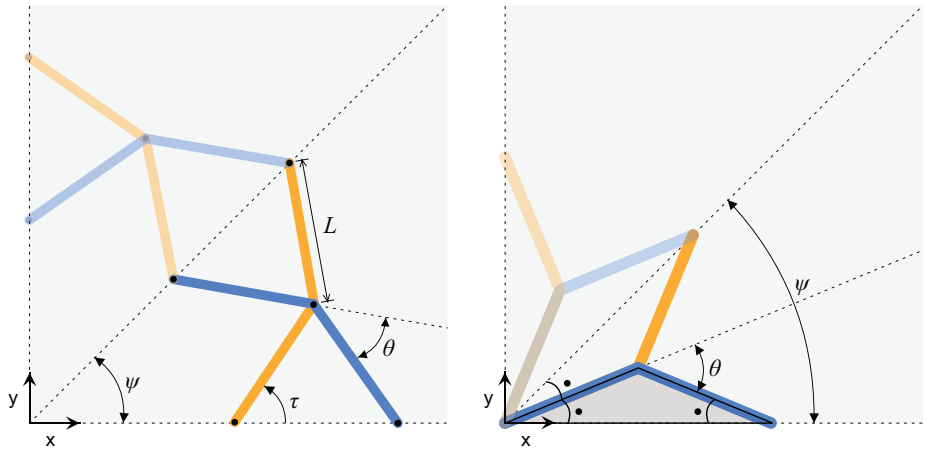

Fig. 3. (a) Constant parameters describing the geometry: L, θ and ψ. State variable describing the mechanism configuration: τ. (b) Relation between link angle θ and sector angle ψ.

measured along the direction of actuation, as shown in Fig. 2 (b). The *ROM* is then calculated as:

$$ROM = \frac{R_2}{R_1}. \tag{2}$$

The *ROM* of a rigid-body radially foldable linkage is uniquely defined by its geometry. However, in compliant mechanisms both the geometry and material properties play a role. For a given geometry the *ROM* is determined by the onset of yield of the material. In this work the emphasis is on investigating the influence of the geometry on the *ROM* rather than the influence of the material properties. The goal is to achieve a *ROM* similar to the *ROM* of the rigid-body radially foldable linkages.

2.2. Kinematics

In literature, plenty of works can be found that explain the mobility of radially foldable linkages and analyse the influence of the shape of the links on the shape of the overall structure [4,5,16–19]. However, the influence of the number of links on the expansion behaviour and the *ROM* is, to the authors knowledge, not described in literature. In this section the analysis is performed for various configurations of Hoberman's linkage as to provide a benchmark for the compliant design.

2.2.1. Parameters

A quadrant of the Hoberman linkage was used as a base model and four parameters define its shape and position. This quadrant consists of two coupled scissor mechanisms and can be seen in Fig. 3 (a). The link angle θ describes the geometry of a link, together with the length L. Furthermore, the angle ψ is shown, which defines the constant sector that the scissor mechanism operates within. Finally, the angle τ is used to describe the position of the links in the mechanism. In this work only linkages with double symmetry are investigated since these can be divided into four similar quadrants, which allows

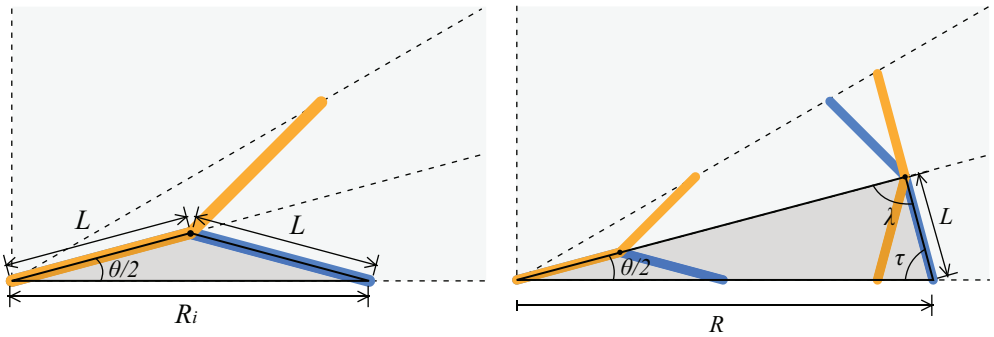

Fig. 4. (a) Initial configuration of a quadrant of the Hoberman linkage. (b) The same quadrant shown in both the initial and expanded configuration.

for convenient modelling. The angle ψ can then be expressed as a function of the number of scissors n_{sc} in a quadrant of the linkage:

$$\psi = \frac{\pi}{2n_{sc}}. \tag{3}$$

By looking at a folded scissor as shown in Fig. 3 (b) and by applying the outside corner theorem, it can be found that the angles θ and ψ are equal.

2.2.2. Expansion behaviour

The expansion ratio ρ describes the state of expansion of the mechanism. It's largest attainable value is equal to the *ROM*. The expansion ratio can be found by comparing the current radius of the mechanism R, with the radius of the mechanism in its fully folded state, R_i.

$$\rho = \frac{R}{R_i}, \tag{4}$$

where the radii are measured along a horizontal axis as can be seen in Fig. 4.

The value of R_i can be derived based on the notion that the links of the scissor form an isosceles triangle in the folded configuration, as can be seen in Fig. 4 (a). This yields:

$$R_i = 2L\cos\left(\frac{\theta}{2}\right). \tag{5}$$

By inspecting the triangle in Fig. 4 (b), the radius of the mechanism in any arbitrary state can be found. The angle θ and L are known, which allows one to obtain the expression for R in terms of the angle λ using the sine rule:

$$\frac{R}{\sin(\lambda)} = \frac{L}{\sin(\frac{\theta}{2})}. \tag{6}$$

Rewriting and expanding the terms yields:

$$R = L\frac{\sin(\lambda)}{\sin(\frac{\theta}{2})} = L\frac{\sin\left(\pi - \frac{\theta}{2} - \tau\right)}{\sin(\frac{\theta}{2})}. \tag{7}$$

Inserting Eq. (5) and Eq. (7) in Eq. (4) and substituting Eq. (3) for θ provides the expansion ratio for a certain angle τ:

$$\rho = \frac{\sin\left(\pi - \frac{\pi}{4n_{sc}} - \tau\right)}{2\sin(\frac{\pi}{4n_{sc}})\cos\left(\frac{\pi}{4n_{sc}}\right)} = \frac{\sin\left(\pi - \frac{\pi}{4n_{sc}} - \tau\right)}{\sin(\frac{\pi}{2n_{sc}})}. \tag{8}$$

With this knowledge it's possible to plot the expansion behaviour for various configurations of the mechanism, as shown in Fig. 5. If the number of scissors per quadrant of the mechanism is increased, the rate of expansion also increases. Hence, in a compliant design where rotations are limited by yielding of the material, it would make sense to incorporate more scissors, because for the same rotation angle τ a larger expansion is obtained.

2.2.3. Range of motion

The *ROM* can be derived from Eq. (8) by noting that the radius of a given mechanism is largest when the sine term in the numerator is equal to one. This occurs for a specific value of τ:

$$\tau = \frac{\pi}{2} - \frac{\pi}{4n_{sc}}. \tag{9}$$

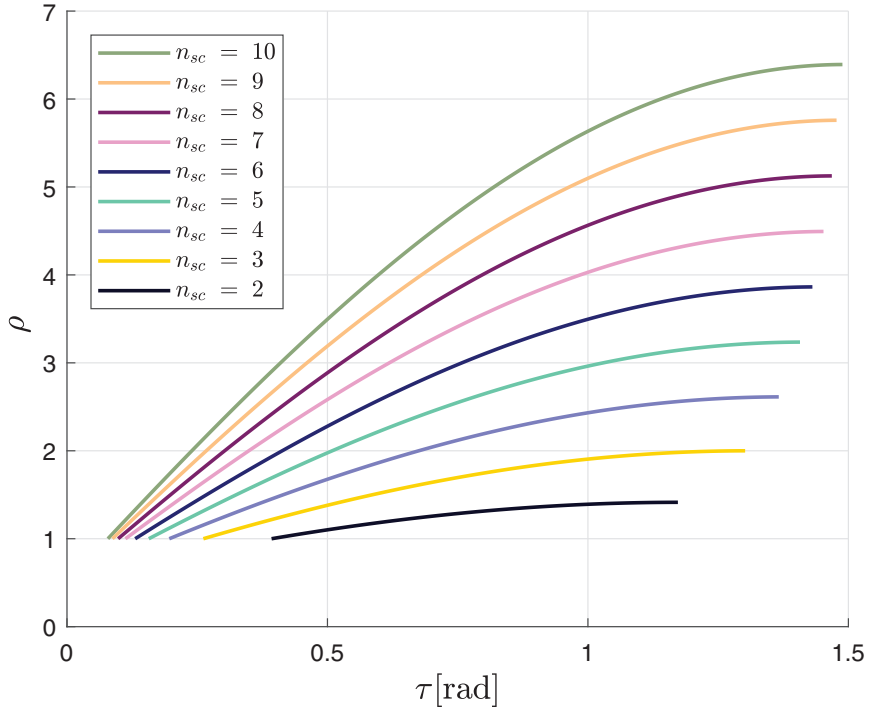

Fig. 5. Expansion behaviour for various configurations of the mechanims.

For this value of τ, which only depends on the number of scissors in the mechanism, the *ROM* is then given by:

$$ROM = \frac{1}{\sin(\frac{\pi}{2n_{sc}})}. \tag{10}$$

Fig. 6 shows the *ROM* for various values of n_{sc}. As it can be observed, the range of motion increases in an approximately linear fashion with the number of scissors per quadrant of the mechanism. This would also argue for increasing the number of scissors in a compliant design in order to obtain a larger *ROM*.

2.3. The compliant design

This section highlights the choices that were made in the design process. First the synthesis of a concept based on straight flexures is described. Then a numerical model based on this concept is presented and finally the optimization procedure is explained.

2.3.1. Synthesis

There are in fact two types of joints in a radially foldable linkage that have to be treated separately when considering a compliant design. The first type of joint is the revolute joint that connects two links at their endpoints. The second type of joint connects two links at their center. Fig. 7 (a) indicates both of these joints in the mechanism. From here onward, the first type of joint is called an intermediate joint, since it operates between the scissors and connects them. A few commonly used options for these types of connections are: cross flexures [20], living hinges [21] and small length flexural pivots [22]. A V-shaped variation of the latter is used in the design described in this paper. A benefit of this variation is longer characteristic length of the pivots which increases overall compliance. Fig. 7 (b) shows how two links, from two different scissors are connected by an intermediate joint.

The second type of joint requires a different approach since in this case both links are connected in their center. Commonly used designs for connecting two bodies in this fashion are split tube flexures or variations of torsion translators [11]. However, these compliant joints become quite long when large deformations are required. If they were applied to a scissor mechanism the links would have to lie in two separate planes with a large distance between them, yielding an impractical mechanism.

The solution proposed in this paper relies on a set of flexures for approximating the behaviour of a rotational joint. Fig. 8 (a) and (b) show how the angled links are suspended between two flexures that exist in the same plane. The flexures subtend the same angle θ as the links. The links can now effectively rotate among their center while displacements of the center are constrained. Both of the links in Fig. 8 can be combined by stacking them on top of each other and connecting

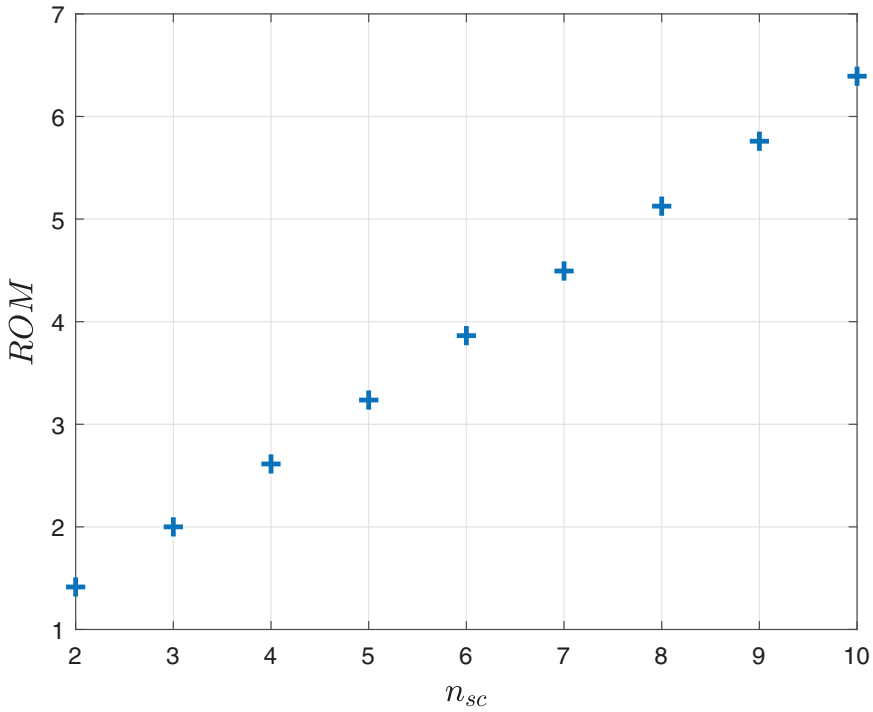

Fig. 6. The relation between the range of motion and the number of scissors per quadrant.

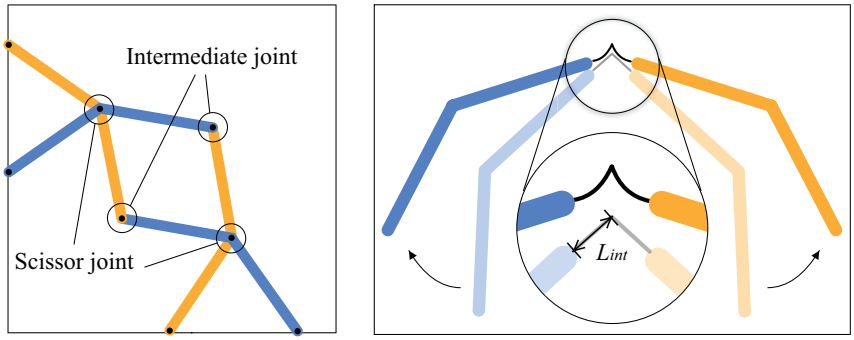

Fig. 7. (a) The two joint types in the mechanism: 'intermediate' and 'scissor'. (b) Depiction of the intermediate joint, formed by a small length flexural pivot, L_{int} is the characteristic length of the pivot.

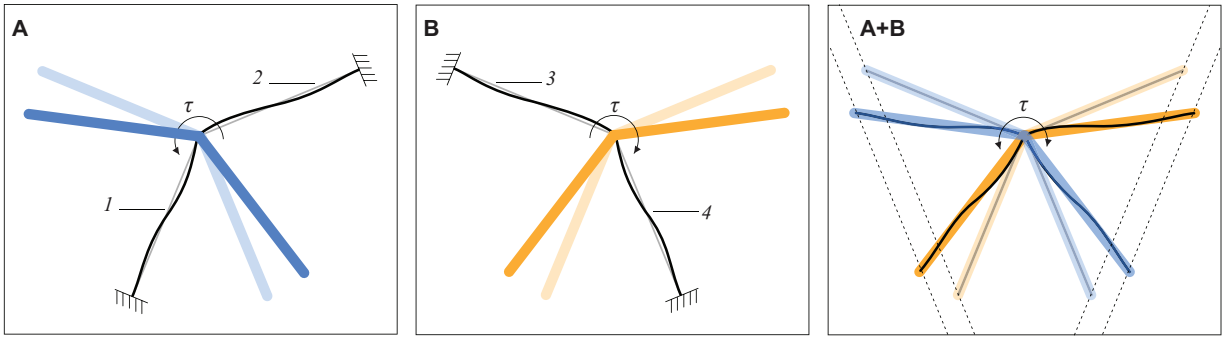

Fig. 8. (a) and (b) show the separate links of the scissor in a neutral and rotated configuration, respectively. Combining the links results in the scissor mechanism shown in (c). It should be noted that the radial lines through the endpoints of the scissor maintain a constant angle. The flexures are numbered for future reference.

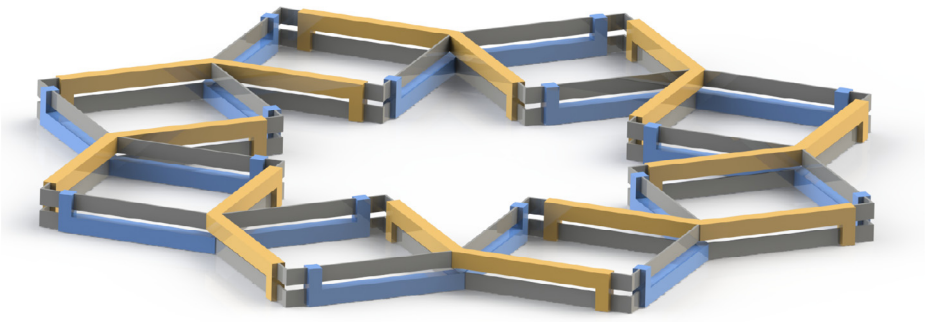

Fig. 9. A CAD-model of the compliant shape-preserving ring. In this image the flexures do not have an initial curvature. The compliant elements are indicated in grey.

the base of the flexures of one link to the endpoints of the other link and vice versa. The resulting mechanism allows the two links to rotate with respect to each other among their center.

Connecting these scissor mechanisms using the intermediate joints results in a double layer closed loop structure resembling the Hoberman linkage. Fig. 9 shows a CAD-representation of this mechanism.

2.3.2. Shape optimization

A shape optimization procedure was used to further shape the flexures in the concept mechanism and generate a design with the desired shape-preserving behaviour. This section describes the finite-element model and the optimization procedure that were used.

Finite-element model The basis for the optimization procedure was formed by a finite-element model of the design described in Section 2.3.1. To build this model, a co-rotational beam element [23] with the ability to handle large displacements was used in combination with a linear isotropic material model. After taking note of the symmetry in the design, only one quadrant of the mechanism was modelled. This reduces the computational cost while still allowing for the computation of the aspect ratio of the compliant system. The nodes at the boundaries of the quadrant are modelled as prismatic joints with a single-degree-of-freedom. To further reduce computational cost, one scissor mechanism is parametrized and then repeated to complete the quadrant. This basic scissor mechanism has four different flexures of constant rectangular cross-section for which both the shape and thickness are parametrized for the optimization procedure. Parametrization of the shape was done by interpolating a set of control points with a B-spline. A piecewise linear approximation of the resulting curve will then form the mesh of the flexure. The distance between the first and the last control point of a flexure remains fixed during optimization and is equal to the length L. The coordinates of the other control points are parameters in the design vector. These coordinates are defined in a local reference frame that has its origin at the starting point of the B-spline. An example of a constructed B-spline can be found in Fig. 10. The height h of these flexures is constant in the optimization. The flexures in the intermediate joints that interconnect the scissor mechanisms have a constant shape, length (L_{int}) and height (h_{int}). However, their thickness is included in the design vector. A distinction in thickness is made between the intermediate joints facing the center of the mechanism and the intermediate joints that face outward, both types receive a different parameter.

Fig. 11 shows a top view of the finite-element model. A stepwise displacement d_p along the y-axis was prescribed for the top node in the model in order to simulate uni-axial straining. In each step the position of the outermost node along the x-axis was measured to determine the aspect ratio of the mechanism. The objective function of the optimization procedure was chosen to be the mean of the errors in the aspect ratio with respect to one:

$$f(\mathbf{X}) = \frac{1}{n_{steps}} \sum_{n=1}^{n_{steps}} |\xi_n - 1|. \tag{11}$$

The number of parameters n_{par} in the design vector $\mathbf{X}$ depends on the number of free control points for each flexure n_{cp}, the number of scissors n_{sc} in the mechanism and the six parameters for the thickness of the compliant elements. The relation is displayed in the following equation:

$$n_{par} = n_{sc} \times (4 \times n_{cp}) + 6. \tag{12}$$

The design vector $\mathbf{X}$ consists of two parts:

$$\mathbf{X} = [\mathbf{x}\ \ \mathbf{T}], \tag{13}$$

where $\mathbf{x}$ is the vector containing the coordinates of the control points for each flexure and $\mathbf{T}$ contains the thickness of the inside-facing and outside-facing intermediate joints (t_{in} and t_{out}), as well as the thickness of each flexure:

$$\mathbf{T} = [t_{in}\ \ t_{out}\ \ t_1\ \ t_2\ \ t_3\ \ t_4]. \tag{14}$$

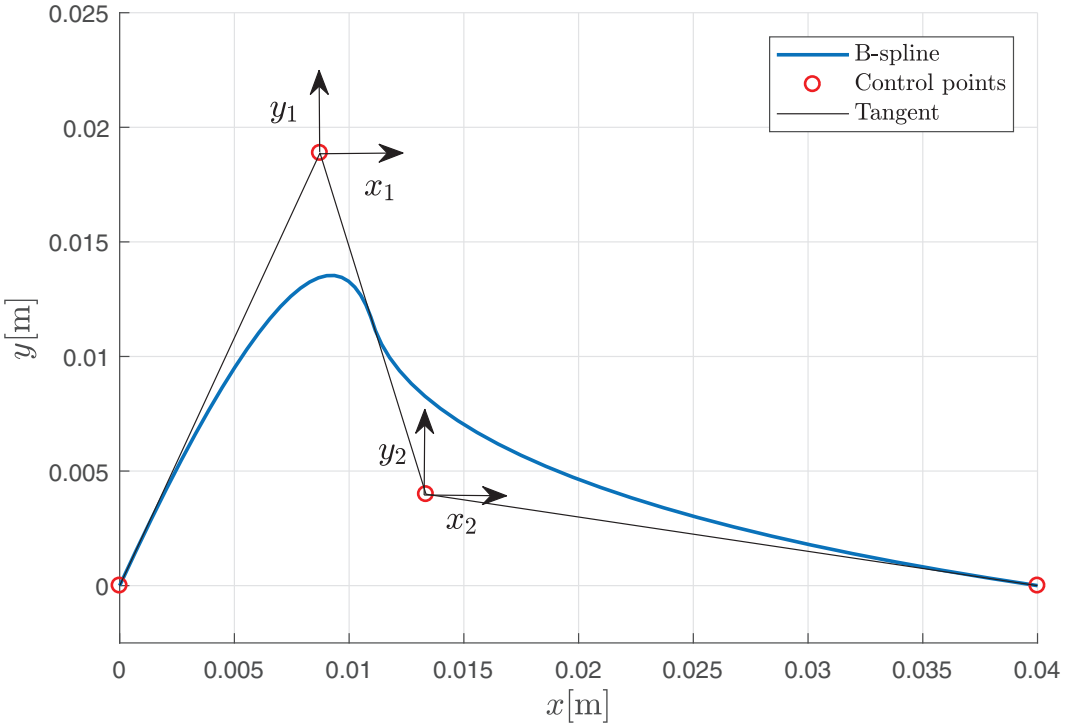

Fig. 10. Two dimensional B-spline interpolation of four control points. The axes indicate the position of the spline and control points. Furthermore, the coordinates of the free control points are shown.

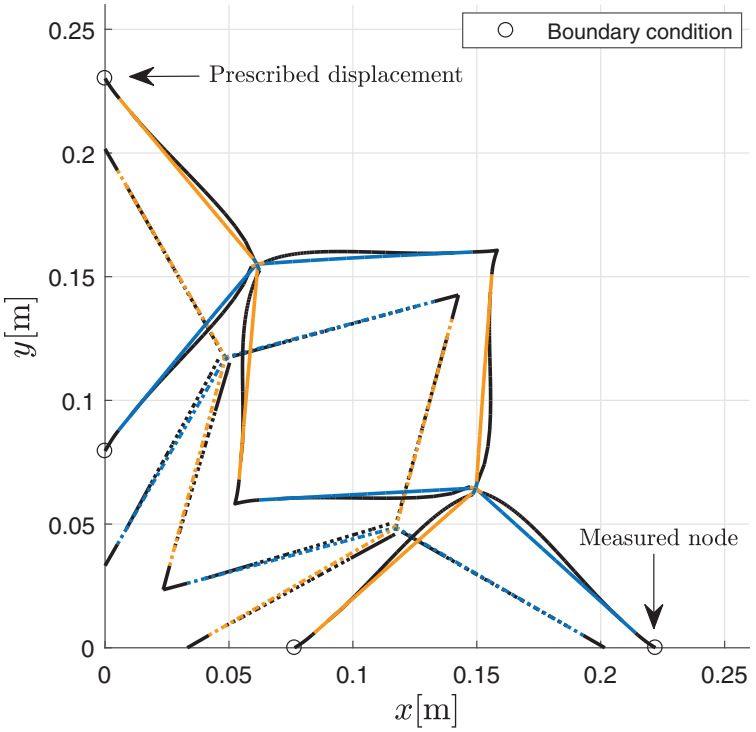

Fig. 11. Top view of the finite element model in both an initial and strained configuration. For clarity only the centerline of each beam-element is displayed. The cross-sectional shape of the elements is not shown. Both the node with a prescribed displacement and the node of which the displacement is measured are indicated.

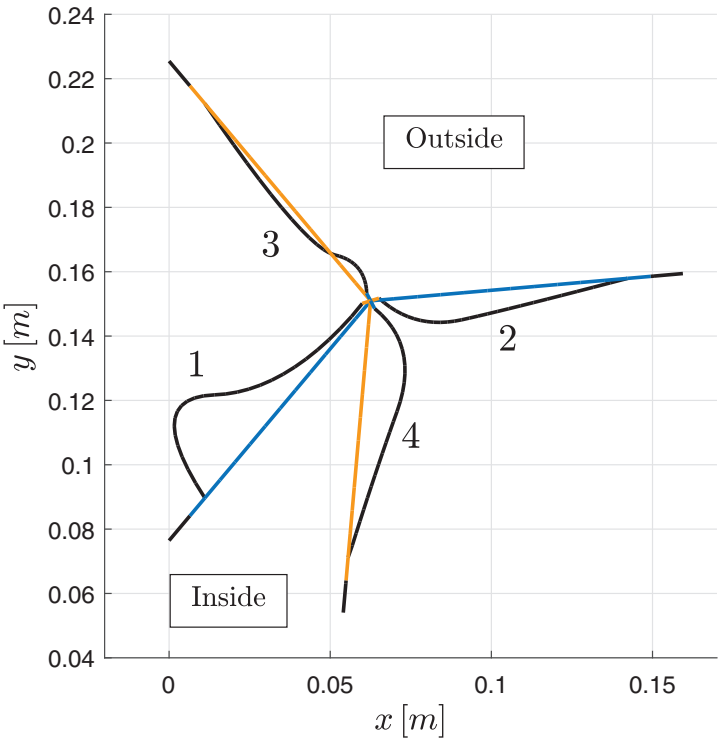

Fig. 12. Numbering convention for the compliant elements in a scissor mechanism. 'Inside' refers to the center of the compliant ring and 'Outside' means facing the external environment.

The numbering convention given in Fig. 12.

Optimization procedure A matlab multistart algorithm was used in combination with a constraint optimization procedure (Matlab function: 'fmincon'). Multistart runs a predefined number of optimization procedures and selects the best local minimum. The design vectors for each starting geometry were drawn from a uniform random distribution and an interior-point method was used to search for an optimum in terms of the design parameters. Furthermore two non-linear constraints were specified to ensure that the results were manufacturable. The first constraint checks the shapes of the B-splines to prevent self intersecting geometries and the second constraint poses a minimal separation distance of $0.1 \times L$ between control points to prevent kinks in the flexure. Both the thickness of the compliant elements and the domain for the control point coordinates is bounded to ensure a manufacturable design.

2.4. Manufacturing

To validate the finite-element model that was used in the optimization procedure a prototype was manufactured using a FFF process. With this fabrication method, the minimum thickness for reliably printing thin-walled features is equal to the nozzle diameter of the printer, in this case: 0.4 mm. Thus, for the prototype, a shape optimization procedure was carried out with a constant thickness t of 0.4 mm for the compliant elements. Moreover, the geometrical parameters were chosen such that the prototype fits on the build plate of the available 3D-printer.

The material used was PETG (Polyethylene terephtalate glycol-modified), because of its toughness and favourable printing properties. The two layers of the design were printed separately and then glued together with a cyanoacrylate glue. This approach circumvents the need for supporting structures of which the removal can damage the thin flexures. Attachment points for testing equipment were printed in conjunction with the mechanism, as can be seen in Fig. 13.

Table 1 contains the coordinates for the control points of the B-splines that define the flexures of the prototype. All other parameters can be found in Table 2.

2.5. Experiments

This section describes the process of testing the fabricated prototype. The main purpose of this testing procedure is validating the model that was used in the optimization procedure. Both the test set-up and measurement procedure are described.

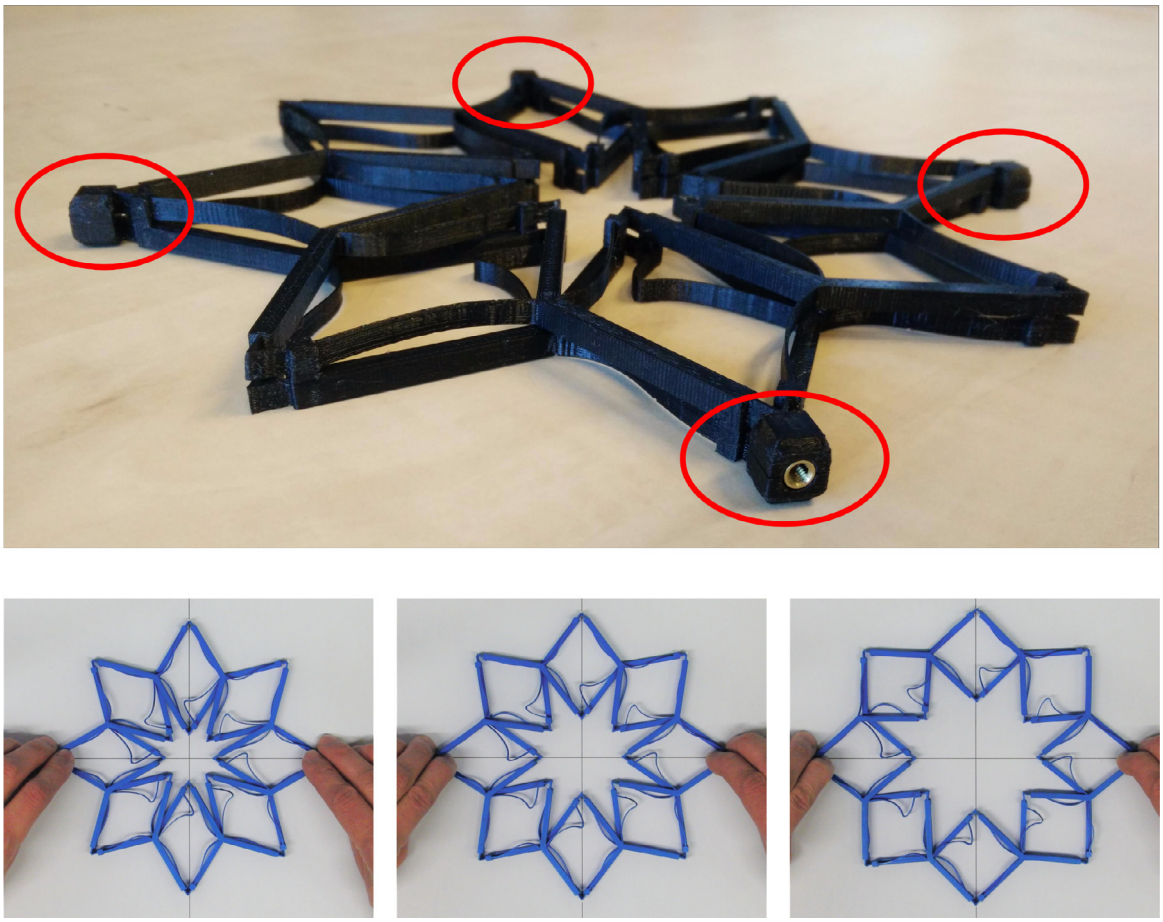

Fig. 13. The picture on the top shows the 3D printed compliant ring, with the integrated nuts for attaching measurement equipment circled in red. The pictures on the bottom show a sequence of top views of the compliant ring in three states of expansion. (For interpretation of the references to colour in this figure legend, the reader is referred to the web version of this article.)

Table 1
Table containing the coordinates of the control points of the flexures that are used in the prototype. The flexures are numbered according to the convention in Fig. 12.

Flexure	Coordinates			
	$x_1\,[m]$	$y_1\,[m]$	$x_2\,[m]$	$y_2\,[m]$
1	0.00837	0.01888	0.01335	0.00399
2	0.00577	−0.00629	0.02596	0.00062
3	0.00796	−0.00233	0.02536	−0.00358
4	0.00543	0.00445	0.02239	0.00250

The experimental set-up is supplied in Fig. 14. The mechanism was strained using a PI M505.4DG linear motor with an accuracy of 1 μm per 25 mm of travel. A Futek (FSH00104) load cell was connected between the prototype and linear motor to measure the actuation force and make sure that the mechanism was unstressed in its initial configuration. The connection between prototype, load cell and motor was done with two pieces of M3 threaded rod. A set of nuts was tightened against the prototype and motor to prevent any backlash in the set-up. Furthermore, the prototype was supported by an acrylate plate to provide a flat surface. Close attention was paid to the vertical alignment of the plate and connector to ensure that the mechanism remained fully supported during the testing. A pin and a piece of threaded rod were used to connect the other end of the prototype to the supporting table beneath the plate.

To validate the finite-element model, the aspect ratio upon expansion was measured. In order to perform these measurements, a stepwise displacement was applied to the prototype using the linear motor. A caliper was then used to measure the diameter of the prototype along both the direction of straining and the transverse direction. From these measurements the aspect ratio upon expansion was calculated.

Table 2
Table containing the parameters that are constant during optimization of the prototype. τ_0 is the value of τ that describes the initial position of the mechanism.

Fixed parameters									
n_{cp}	n_{sc}	τ_0	θ	L	L_{int} [m]	h [m]	h_{int} [m]	t [m]	E [GPa]
2	2	$\pi/6$	$\pi/4$	0.035	0.005	0.004	0.008	0.0004	$2.2e^9$

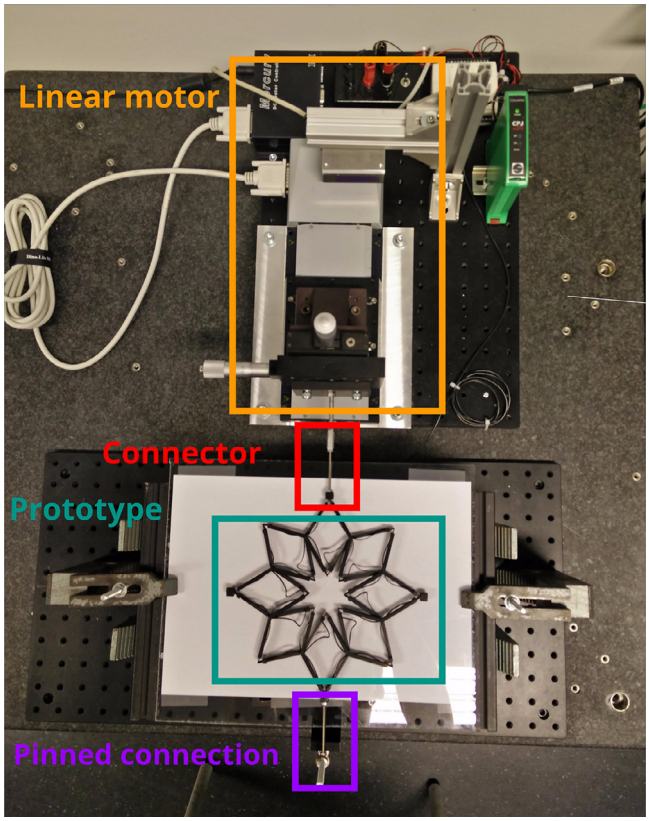

Fig. 14. The test set-up consists of a linear motor (orange), threaded rod connection and load cell (red), threaded rod for clamping the mechanism (purple) and the compliant ring itself (green). (For interpretation of the references to colour in this figure legend, the reader is referred to the web version of this article.)

3. Results and discussion

This section first demonstrates three optimal designs, each with a different numbers of scissor mechanisms. These mechanisms are then compared with their rigid body equivalent mechanisms. Next, the performance of one of the optimal designs is compared numerically with both the unoptimized concept mechanism and a conventional circular ring of a similar size. Lastly, the results of the experimental validation of the finite-element model are shown and discussed.

3.1. Optimal designs

A multistart optimization procedure was performed for a design with two, three and four scissor mechanisms. For each procedure 200 random starting geometries were generated and optimized. The boundary condition loadstep within every evaluation of the finite-element model was applied in 50 steps. For each design the number of free control points for the B-splines was fixed at two.

The best result for the design with two, three and four scissors is shown in Table 3, 4 and 5. Table 6 contains the values of the parameters that are constant for each optimization.

Each design exhibits shape-preserving behaviour along the full range-of-motion with a maximum error in the aspect ratio in the order of 1%. This range-of-motion is in each case limited by the yield strength of the material. Fig. 15 compares the compliant optimal designs and their equivalent rigid body mechanisms (the theoretical maximum *ROM*). Contrary to these rigid body mechanism, the compliant designs cannot be fully folded since the flexures have to be accommodated for.

Table 3
Table containing the results from the optimization procedure for the mechanism with two scissor pairs per quadrant. The graph shows the design in both the initial and expanded configuration.

Two Scissor Mechanisms per Quadrant						
Results	$f(\boldsymbol{X})$	ROM				
	0.001	1.2453				
Parameters	τ_0 $[rad]$	θ $[rad]$				
	$\pi/7$	$\pi/4$				
$\boldsymbol{x}$ $[m]$	x_1	y_1	x_2	y_2		
Flexure 1	0.0048	0.0303	0.0123	0.0034		
Flexure 2	0.0033	-0.0116	0.0561	-0.0052		
Flexure 3	0.0051	0.0198	0.0347	-0.0031		
Flexure 4	0.0012	0.0141	0.0321	0.0103		
$\boldsymbol{T}$ $[mm]$	t_{in}	t_{out}	t_1	t_2	t_3	t_4
	0.5058	0.5106	0.5071	0.5406	0.5071	0.6881

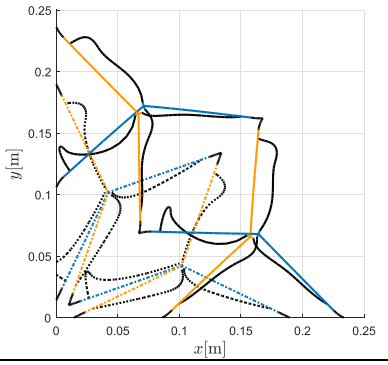

Table 4
Table containing the results from the optimization procedure for the mechanism with three scissor pairs per quadrant. The graph shows the design in both the initial and expanded configuration.

Three Scissor Mechanisms per Quadrant						
Results	$f(\boldsymbol{X})$	ROM				
	0.0007	1.3922				
Parameters	τ_0 $[rad]$	θ $[rad]$				
	$\pi/8.5$	$\pi/6$				
$\boldsymbol{x}$ $[m]$	x_1	y_1	x_2	y_2		
Flexure 1	0.0115	0.0355	0.0420	0.0003		
Flexure 2	0.0101	-0.0108	0.0400	-0.0067		
Flexure 3	0.0541	-0.0057	0.0697	0.0061		
Flexure 4	0.0101	0.0154	0.0521	0.0051		
$\boldsymbol{T}$ $[mm]$	t_{in}	t_{out}	t_1	t_2	t_3	t_4
	0.5002	0.5004	0.5003	0.5486	0.5003	0.6934

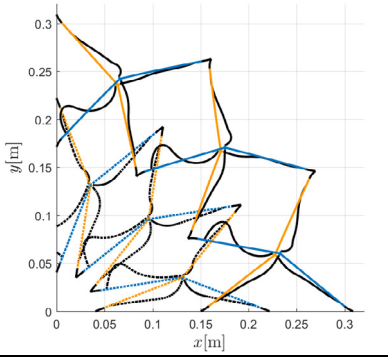

Table 5
Table containing the results from the optimization procedure for the mechanism with four scissor pairs per quadrant. The graph shows the design in both the initial and expanded configuration.

Four Scissor Mechanisms per Quadrant						
Results	$f(\boldsymbol{X})$	ROM				
	0.0011	1.4386				
Parameters	τ_0 $[rad]$	θ $[rad]$				
	$\pi/9.5$	$\pi/8$				
$\boldsymbol{x}$ $[m]$	x_1	y_1	x_2	y_2		
Flexure 1	0.0202	0.0362	0.0278	0.0020		
Flexure 2	0.0156	-0.0099	0.0596	-0.0018		
Flexure 3	0.0685	0.0371	0.0682	-0.0327		
Flexure 4	0.0154	0.0108	0.0595	0.0028		
$\boldsymbol{T}$ $[mm]$	t_{in}	t_{out}	t_1	t_2	t_3	t_4
	0.5021	0.5028	0.5027	0.6133	0.5049	0.7317

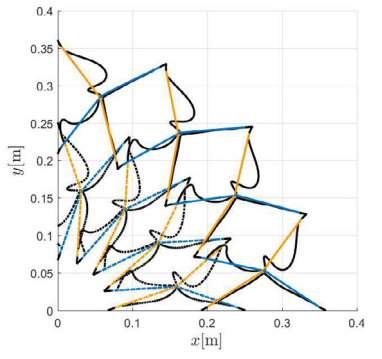

Table 6
Table containing the parameters that are constant for each optimization procedure, regardless of the number of scissor mechanisms.

Fixed parameters				
L [m]	L_{int} [m]	h [m]	h_{int} [m]	E [GPa]
0.08	0.01	0.008	0.0016	$2.2e^9$

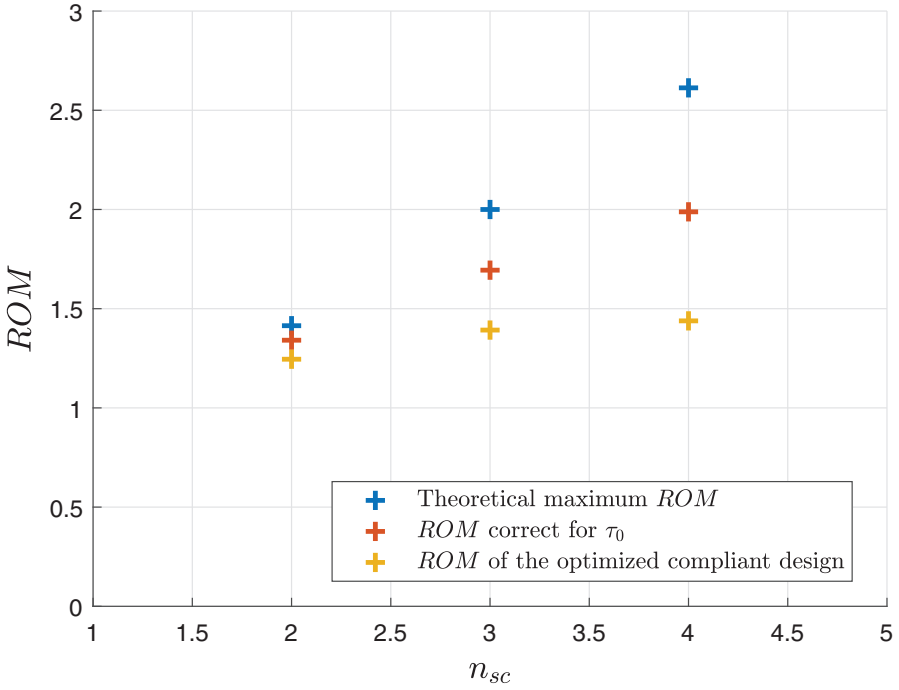

Fig. 15. Comparison between the theoretical maximum *ROM*, the theoretical *ROM* corrected for the initial configuration of the compliant designs, and the *ROM* of the optimization results.

To draw a fair comparison, the *ROM* of the rigid body mechanism is also computed from the same starting configuration as that of the compliant designs. This is done by taking into account the initial angle τ_0 for the starting configuration, using Eq. (7) and Eq. (8).

The *ROM* of the compliant designs tends to increase with the number of scissor mechanisms. However, there is a discrepancy between the *ROM* of the compliant design and its equivalent rigid body mechanism, that also increases with the number of scissor mechanisms. It might be possible to mitigate this effect by enlarging the design space for the optimization. For example through increasing the number of free control points for the B-splines or by using doubly-curved flexures, as in the work of Radaelli & Herder [24]. Moreover, the *ROM* can be increased by choosing a material with a higher yield strength. The design consisting of four scissor mechanisms has the largest *ROM* with a value of 1.44.

3.2. Performance

To understand the performance of the optimal designs, this section shows the results of a finite-element analysis. A comparison is drawn between the optimal design with two scissor mechanism, the concept mechanism with straight flexures and a regular thin-walled ring. The regular thin-walled ring is included in this analysis to have a conventional structure as a benchmark for evaluating the shape-preserving qualities of the design.

The concept design is geometrically similar to the optimized design, except for the fact that all its flexures are straight and have a thickness of 0.5 mm. The undeformed thin-walled ring has a radius of 190 mm which is similar to the outer radius of the designs. Furthermore its shell has a thickness of 1 mm and a height of 10 mm. For each analysis the same PETG material properties were used and each mechanism was strained until the first element reached the yield strength of $\approx$ 53 MPa. Fig. 16 shows the mechanisms and ring in their strained and unstrained configurations.

Fig. 17 shows the aspect ratio upon expansion of the mechanisms. The mechanisms clearly follow a different trend than the thin-walled ring. The optimized design has an aspect ratio that is only slightly better than the unoptimized concept. However, the optimization procedure has extended the *ROM* of the concept by 63%. Furthermore, it is shown that the opti-

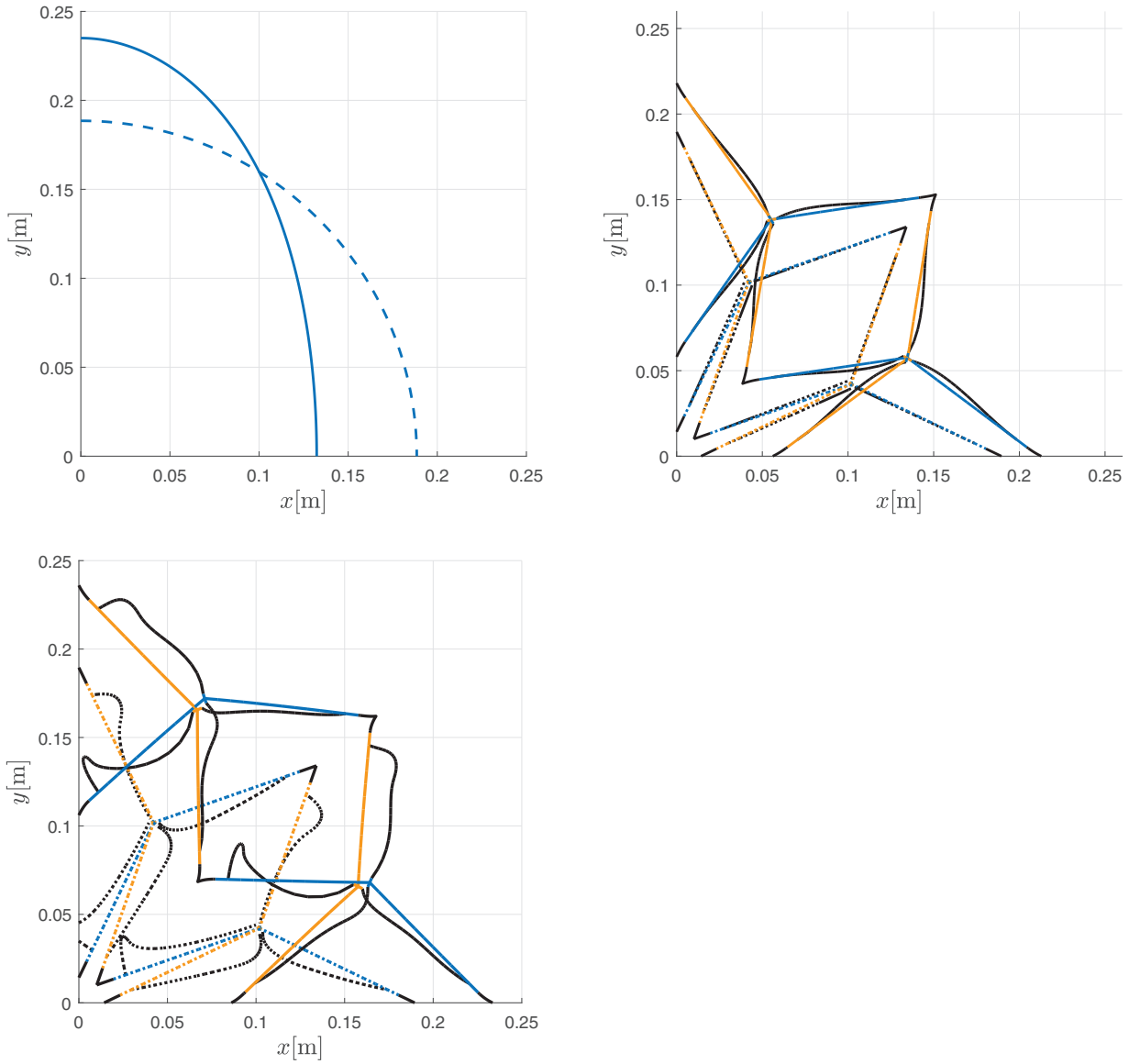

Fig. 16. Comparison between deformed and undeformed configurations under uni-axial loading: (a) quadrant of the thin-walled ring made of PETG; (b) a quadrant of the concept mechanism; (c) a quadrant of the optimized compliant mechanism. Deformed and undeformed states are shown by bold and dotted lines, respectively.

mized design preserves its shape up to 99%, which translates to an aspect ratio that is 75% higher than the aspect ratio of the conventional ring at the end of its *ROM*.

3.3. Experimental results

First the thickness of each compliant element in the prototype was measured with a caliper (resolution of 0.05 mm). This demonstrated a large discrepancy between the intended thickness of the flexures and the actual thickness. The measurements were averaged for each type of flexure which gave the following result for the vector **T**:

$$\mathbf{T} = [0.6 \;\; 0.55 \;\; 0.6 \;\; 0.6 \;\; 0.55 \;\; 0.6] \text{ mm}. \tag{15}$$

A calibrated finite-element analysis was then performed with this corrected **T** to provide a better means of comparison with the results of the experiment. The measurements in the experiment were conducted in fivefold on the prototype described in Section 2.4. To compare the finite-element model and prototype the displacement prescribed to the model has to be doubled for the same aspect ratio, since the finite-element model considers only one quadrant of the mechanism. Fig. 18 shows the obtained results for the aspect ratio upon expansion. Both the calibrated finite-element model and the optimal finite-element model are shown. The prototype preserves its shape up to 88% at full expansion.

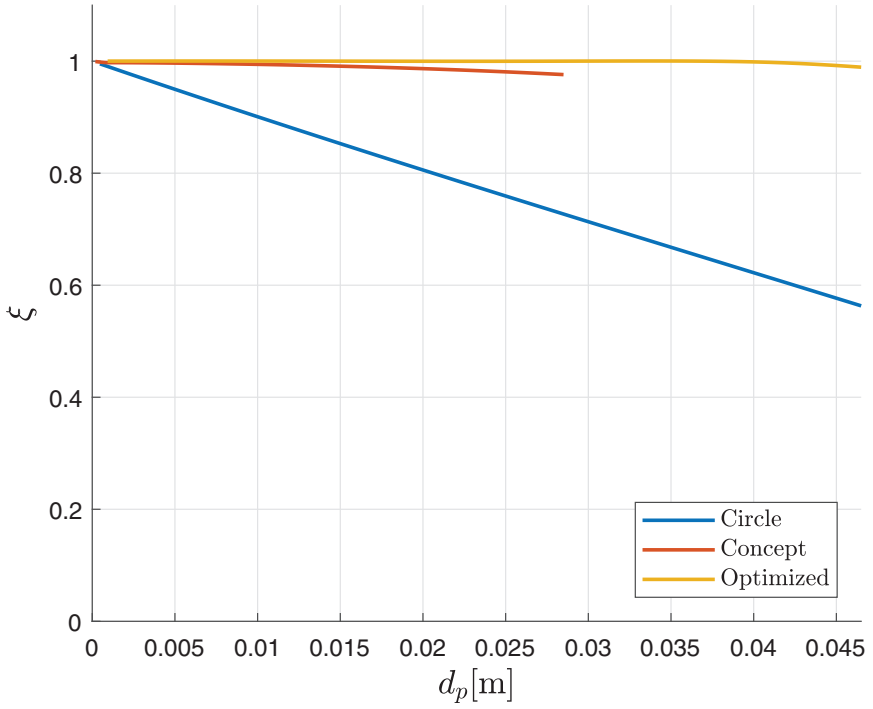

Fig. 17. Comparison between the aspect ratio of the thin-walled ring versus the concept and optimized compliant designs.

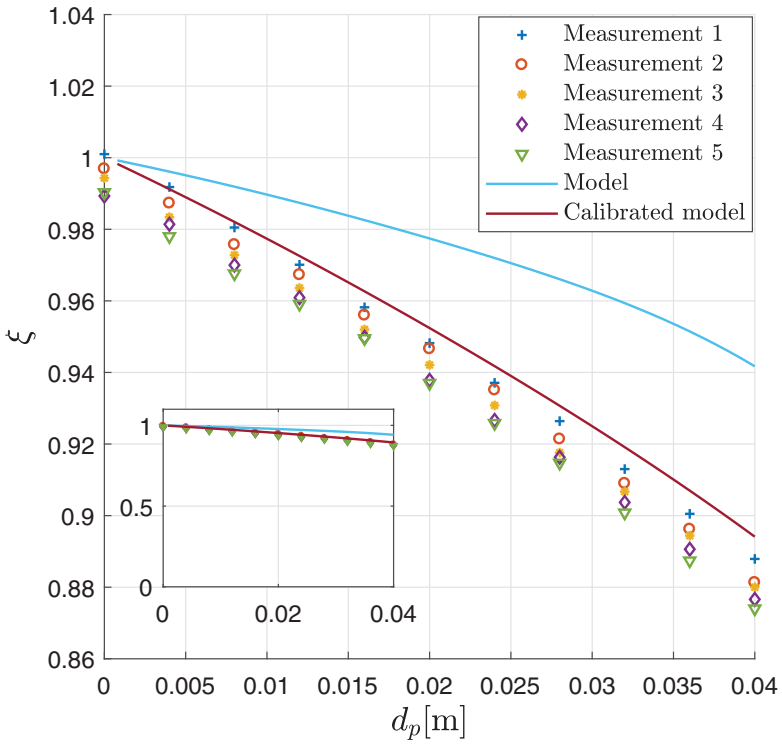

Fig. 18. Comparison between measurement results, finite-element model and calibrated finite-element model. The inset displays the same results but also shows zero on the y-axis.

The measurements are in good agreement with the calibrated model. However, it should be noted that the aspect ratio is decreasing slightly for each consecutive set of measurements. This could indicate that some yielding is occurring upon straining of the mechanism even though this was not predicted by the model. Hence the experiments do not validate the numerical model in itâs entirety and the use of a more sophisticated material model might be warranted when the mechanism has to undergo multiple loading cycles. Moreover, the observed behaviour could be an effect of the fabrication method used, since 3D printed structures are generally an-isotropic and non-homogenous in nature.

The mechanism consists of two layers that are printed separately and glued together. Maintaining alignment of these two layers while gluing proved challenging. Errors in the alignment will surely have an influence on the behaviour of the mechanism and this could, to some extent, also explain the discrepancies between the calibrated model and the experimental results.

3.4. The scissor mechanism

The flexure based rotational joint at the center of the compliant scissor mechanism can be a very versatile building block for the design of other compliant mechanisms. Both the shape and thickness of the flexures can be varied as well as the internal angle θ of the elements in the scissor. This allows for a lot of freedom in tuning both the overall shape of a mechanism based on this scissor element, as well as its expansion behaviour. Moreover, the shape optimization procedure used in this work could also be used to tune the load-displacement characteristic of a mechanism. This further extends the possibilities of applying this scissor element in practical applications.

4. Conclusion

To the authors' knowledge, this paper has presented the first design of a compliant shape-preserving ring. Four variations of the design have been created. Three of these designs had a maximum deviation from the desired aspect ratio of only 1%, which was proved to be an increase in performance of 75% over a conventional thin-walled ring.

The fourth design was scaled and optimized for fabrication. A prototype of this design has been realized from PETG by using a fused-filament-fabrication method and an experimental evaluation of this prototype demonstrated good agreement with the finite-element model. This puts confidence in the designs presented in the paper.

In order to realize the design of the compliant shape-preserving ring, a novel compliant scissor mechanism has been developed. This mechanism can be used as a building block in other compliant (shape-preserving) mechanisms due to the possibilities for tuning its mechanical properties.

Declaration of Competing Interest

The authors declare that they do not have any financial or nonfinancial conflict of interests.

Acknowledgement

The authors would like to acknowledge financial support from 3mE, TU Delft, SHELL - TEVAR cohesion project.

References

[1] F. Broeren, W. van de Sandel, V. van der Wijk, J. Herder, Dilational triangulated shells using pantographs, in: 2018 International Conference on Reconfigurable Mechanisms and Robots (ReMAR), IEEE, 2018, pp. 1–6.
[2] G.E. Fenci, N.G. Currie, Deployable structures classification: a review, Int. J. Space Struct. 32 (2) (2017) 112–130.
[3] E.R. Adrover, Deployable Structures, Laurence King Publishing London, 2015.
[4] C. Hoberman, Reversibly expandable doubly-curved truss structure, 1990,.
[5] Z. You, S. Pellegrino, Foldable bar structures, Int. J. Solids Struct. 34 (15) (1997) 1825–1847, doi:10.1016/S0020-7683(96)00125-4.
[6] K. Wohlhart, Regular polyhedral linkages, in: 2nd Workshop on Computational Kinematics, Seoul, Korea, 2001, pp. 4–6.
[7] K. Wohlhart, Irregular polyhedral linkages, in: Proc. of the 11th World Congress in Mechanism and Machine Science, Tianjin, China, 2004, pp. 1083–1087.
[8] G. Wei, Y. Chen, J. Dai, Synthesis, mobility, and multifurcation of deployable polyhedral mechanisms with radially reciprocating motion, J. Mech. Des. 136 (9) (2014) 1003–1012, doi:10.1115/1.4027638.
[9] G. Kiper, E. Söylemez, A.Ö. Kişisel, A family of deployable polygons and polyhedra, Mech. Mach. Theory 43 (5) (2008) 627–640.
[10] G. Kiper, E. Söylemez, Polyhedral linkages obtained as assemblies of planar link groups, Front. Mech. Eng. 8 (1) (2013) 3–9.
[11] L. Howell, S. Magleby, B. Olsen, The Handbook of Compliant Mechanisms, John Wiley and Sons Inc., Chichester, UK, 2013.
[12] J. Shim, C. Perdigou, E. Chen, K. Bertoldi, P. Reis, Buckling-induced encapsulation of structured elastic shells under pressure, Proc. Natl. Acad. Sci. 109 (16) (2012) 5978–5983, doi:10.1073/pnas.1115674109.
[13] K. Bertoldi, P.M. Reis, S. Willshaw, T. Mullin, Negative Poisson's ratio behavior induced by an elastic instability, Adv. Mater. 22 (3) (2010) 361–366.
[14] G.W. Milton, New examples of three-dimensional dilational materials, Physica Status Solidi (b) 252 (7) (2015) 1426–1430.
[15] U.D. Larsen, O. Sigmund, S. Bouwstra, Design and fabrication of compliant micromechanisms and structures with negative Poissons ratio, J. Microelectromech. Syst. 6 (2) (1997).
[16] C. Hoberman, Radial expansion/retraction truss structures, 1991.
[17] J. Patel, G.K. Ananthasuresh, A kinematic theory for radially foldable planar linkages, Int. J. Solids Struct. 44 (18–19) (2007) 6279–6298, doi:10.1016/j.ijsolstr.2007.02.023.
[18] J. Cai, J. Feng, Y. Xu, Kinematic analysis of hoberman's linkages with the screw theory, Mech. Mach. Theory 63 (2013) 28–34, doi:10.1016/j.mechmachtheory.2013.01.004.

[19] J. Cai, X. Deng, J. Feng, Y. Xu, Mobility analysis of generalized angulated scissor-like elements with the reciprocal screw theory, Mech. Mach. Theory 82 (2014) 256–265, doi:10.1016/j.mechmachtheory.2014.07.011.
[20] B.D. Jensen, L.L. Howell, The modeling of cross-axis flexural pivots, Mech. Mach. Theory 37 (5) (2002) 461–476, doi:10.1016/S0094-114X(02)00007-1.
[21] L. Howell, Compliant Mechanisms, John Wiley and Sons Inc., New York,US, 2001.
[22] L.L. Howell, A. Midha, A method for the design of compliant mechanisms with small-length flexural pivots, J. Mech. Des. 116 (1) (1994) 280–290.
[23] J.-M. Battini, Co-rotational Beam Elements in Instability Problems, KTH, 2002 Ph.D. thesis.
[24] G. Radaelli, J. Herder, Gravity balanced compliant shell mechanisms, Int. J. Solids Struct. 118 (2017) 78–88.